REGULAR PAPER
DOI: 10.1007/s12541-017-0060-1
ISSN 2234-7593 (Print) / 2005-4602 (Online)

Stiffness Modeling and Optimization of a 3-DOF Parallel Robot in a Serial-Parallel Polishing Machine

Peng Xu[1,2], Bing Li[1,#], Chi-Fai Cheung[2], and Ju-Fan Zhang[1]

1 School of Mechanical Engineering and Automation, Shenzhen Graduate School, Harbin Institute of Technology, Xili, Nanshan, Shenzhen, 518055, China
2 Partner State Key Laboratory of Ultra-Precision Machining Technology, Department of Industrial and Systems Engineering, The Hong Kong Polytechnic University, Hung Hom, Kowloon, Hong Kong, 999077, China
Corresponding Author / E-mail: libing.sgs@hit.edu.cn, TEL: +86-755-2603-3485, FAX: +86-755-2603-3485

KEYWORDS: Polishing machine, Parallel robot, Stiffness, Optimization

Polishing is a kind of finishing process that can effectively reduce the surface defects and improve the form accuracy. This paper presents a novel hybrid machine with 6 degrees of freedom (DOF) serial-parallel topological structure used as an ultra-precision polishing equipment which is composed of a 3-DOF parallel robot, a 2-DOF serial robot and a turntable providing a redundant DOF. Due to the complexity of structure, stiffness performance evaluation of the parallel robot becomes a challenge. As a result, a theoretical model of the parallel robot based on the virtual work principle and the deformation superposition principle is formulated for analyzing the stiffness performance. With the developed model, a multi-objective dimensional optimization method is developed to maximize both the workspace volume and the global stiffness performance of the parallel robot. Artificial intelligence approach based on genetic algorithms is implemented to obtain an optimal combination of structural parameters. The effectiveness of this method is validated by simulation and the parallel robot with optimized structural parameters has a workspace with higher stiffness performance, hence justifies its suitability for high precision polishing.

Manuscript received: March 9, 2016 / Revised: October 7, 2016 / Accepted: December 12, 2016

1. Introduction

Polishing is an important final processing step for precision machining to remove materials and subsurface damage so as to achieve better form accuracy and surface finish of the workpiece. It is vital for ensuring the surface quality which directly affects the functional performance, appearance and longevity of the workpiece surfaces.[1,2] With the rapid development of technology in recent years, more complicated freeform surfaces and new materials have been employed.[3] It is more difficult to polish those surfaces manually by skillful workers based the traditional polishing method. As a result, automatic polishing technology is clearly the way forward to achieve a sustainable freeform surface with high efficiency and reliability.

Most of the polishing machines used for fabrication of freeform surfaces are based on the conventional 5-axis machine tool structure[4-6] or the industrial robot structure.[7-10] In precision machining, a new type of machine as referred to as parallel kinematic machine, has been proven successful and advanced.[11-13] The parallel kinematic machine has some favorable characteristics compared to the traditional machine tool and robot with serial topological structure, such as high rigidity, good dynamic performance, superior accuracy, low mobile masses and greater load-to-weight ratio. In this paper, a novel polishing machine with serial-parallel mechanism is presented which provides features of both serial and parallel robots.

Stiffness is related to the accuracy of a parallel robot since it reflects the direct mapping between the externally applied wrench and the deformation twist of the end-effector.[14-16] It is one of the utmost important properties, which is particularly true for those which are used as precision equipment, since higher stiffness allows more accurate positioning with a certain external wrench. Although parallel robots show good performance in terms of rigidity and accuracy, it is still necessary to analysis, evaluate and optimize the stiffness performance in the preliminary design stage.

Stiffness analysis of parallel robot has attracted a lot of attention from researchers and there are several methods to establish the stiffness model. Klimchiks et al.[17] divided the modeling approaches of stiffness into three main groups: the finite elements analysis, the matrix structural analysis, and the virtual joint modeling method. Yan et al.[18] divided the analysis methods into three categories from other different perspectives which include: experimental method, finite element analysis method and algebraic analytical method. In this study, the stiffness is established for relating the component stiffness to the parallel robot stiffness by using the algebraic analytical method.

The stiffness of the parallel robot has not only close relationship with the component stiffness, but also with that of its structural parameters. Optimization design should be conducted aiming at improving the stiffness performance by adjusting the structural parameters. Many researchers have studied on the issue of stiffness optimal design of parallel robot.[19-21] Another key performance for parallel robots is their work space volume.[22,23] However, the objectives may conflict with each other. As a result, a multi-objective optimization model should be carried out to ensure that both workspace volume and global stiffness performance of the parallel robot satisfy the requirements. Optimization design of multi-domain engineering systems can be rather complex and it requires an integrated and concurrent approach in order to obtain the optimal results. Recently, some artificial intelligence approaches based on global search approach, such as Genetic Algorithm (GA), Particle Swarm Optimization (PSO) and Simulated Annealing (SA) have been increasingly used to carry out the optimization solution of the mechanisms.[24-27] GA generates solutions to optimize the problems using techniques inspired by natural evolution, such as inheritance, mutation, selection and crossover. It is by far the most widely used algorithms in evolutionary algorithms. Considering that the optimization problem of the designed parallel robot has highly nonlinear characteristics, the GA is selected to solve this problem due to its good adequacy with the complicated optimization problem.

The reminder of the paper is organized as follows. In section 2, the concept of a novel serial-parallel polishing machine tool is presented. Section 3 deals with the kinematics model. Section 4 discusses the establishment of the stiffness model. The optimization model is studied in Section 5. Section 6 focuses on the analysis of the results and discussion. Finally, conclusions are given in Section 7.

2. Conceptual Design of the Polishing Machine

As shown in Fig. 1, a polishing strategy called precession polishing process,[28] is adopted in the proposed polishing machine. It is different from the traditional polishing process in which the polishing tool is rotated vertically to the local normal direction of surface while the rotation-axis of the polishing tool is inclined to the part surface's local normal direction. To obtain a uniform surface texture demonstrating no directional properties, the tool axis is then precessed about the local normal direction of the surface.

To polish a freeform surface, the machine tool should possess five-axis motions, including three translational DOF and two rotational DOF. Currently, most of the five-axis hybrid mechanism are used in milling machine.[13,29-31] As one of a flexible machining technologies, the material removal in polishing process is different from milling process, which depends on not only the tool path and the tool size, but also pressure and the velocity distribution on the contact area and the dwell time. Lin et al.[2,12] proposed a polishing machine which consists of a variation of the METROM Pentapod parallel robot and a numerical control rotary table. Kakinuma et al.[32] designed a portable polishing machine based on the concept of integrating a 3-PRS parallel robot and

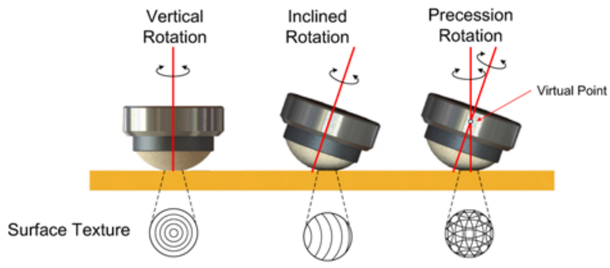

Fig. 1 Precessions polishing process

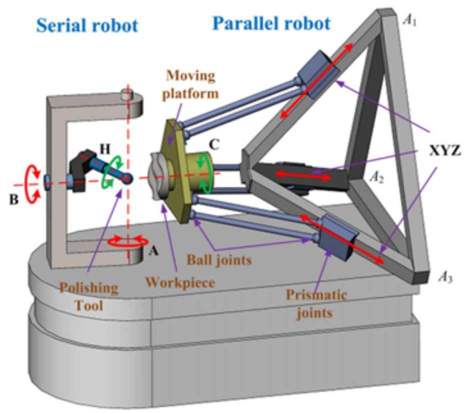

(a) Configuration of the polishing machine

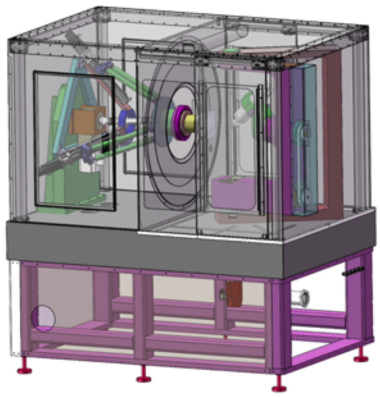

(b) 3D model of the polishing machine

Fig. 2 Serial-parallel polishing machine

a 2-DOF translational component. Liao et al.[33] developed a polishing system with a similar mechanism. However, by simply replacing the tool head, most of the hybrid mechanisms used in the previous polishing machines are learnt from milling machines. As a result, the polishing tool can only achieve motions in milling process which usually leads to polishing processes with vertical or inclined tool rotation as shown in Fig. 1. Very few attentions have been paid on the development of hybrid mechanisms which are particularly suitable for polishing process.

This paper adopts precession polishing process, which is an enabling technology to achieve more uniform surface texture. As most of the existing hybrid mechanisms have coupled motions between translations and rotations, the relative positon between the tool and the workpiece usually comes 'contaminated' by angular motions, which have to be compensated by the motions in the translational axes. In this study, considering the motion characteristic of the precession motion, it is easier to accomplish the precession motion by a two-axis rotatory table (serial robot) rather than a parallel robot. The complex precession motion is accomplished through a special mechanical design and a simple control algorithm. As the serial robot provides two rotations, the parallel robot is required to provide three translations. According to Merlet,[34] a group of parallel robot called Delta which can provide three translations have been intensively tested and successfully commercialized. By intersecting the linear guide to a vertex, the stiffness of the fixed base in the Delta parallel robot can be improved. Although this may reduce the distance of travel along the Z direction, there is little effect on the processing capacity of the polishing machine, because the workpiece to be polished usually has a large diameter and a small height. Finally, the proposed serial-parallel polishing machine is shown in Fig. 2, which is a serial-parallel hybrid mechanism consists of a serial robot and a parallel robot.

The serial robot consists of a rotating/tilting table (A and B axes) and a polishing tool spindle (H axis). The rotating axis A is vertical and the tilting axis B is horizontal to the base. A and B motions enable H to rotate around two orthogonal axes. The curvature center of polishing tool (Bonnet) is coincided with the virtual pivot intersected by the two axes.

The moving platform of the parallel robot is connected to the base by three identical serial chains. Each of the three chains contains one spatial parallelogram, the vertices of which are four ball joints. Each parallelogram is connected to the base by a prismatic joint. The parallel robot has 3-DOF, so it requires three actuators. The ball joints are passive joints and the prismatic joints are active joints. As a result, the output of the moving platform (X, Y and Z translation axes) can be obtained through a combination of the actuation to the three prismatic joints. When the motions of the prismatic joints are fixed, the moving platform can be fixed during the polishing process. A turntable (C axis) that holds the workpiece is mounted on the moving platform. It can be rotated to provide a rotational motion of the workpiece when symmetric surfaces are axially polished.

Since the three rotational axes of the serial module intersect at a virtual pivot, pure rotations in A and B preserve the same polishing contact area between the polishing tool and the workpiece, causing no XYZ translations. As a result, the motions are decoupled. The positions of the polishing spot are all controlled by the parallel robot and the orientations of the surface texture on the spot are all determined by the serial robot. This motion decoupled feature provides the benefit for the development of control algorithm.

Due to the complexity of structure, the stiffness performance of the parallel robot in the serial-parallel polishing machine is the focus of this study. It must be noted that there are already some researchers analyzing the stiffness characteristics of the similar parallel robot. Company and Pierrot[35] built a simplified stiffness model by taking into account of both the effect of actuators and rods stiffness. Yan et al.[18] established a stiffness model with a strain energy method by considering the compliances of mobile platform, leg and actuator. However, these models may produce inaccurate results in the evaluation of the stiffness performance of a parallel robot for a precision machining equipment.

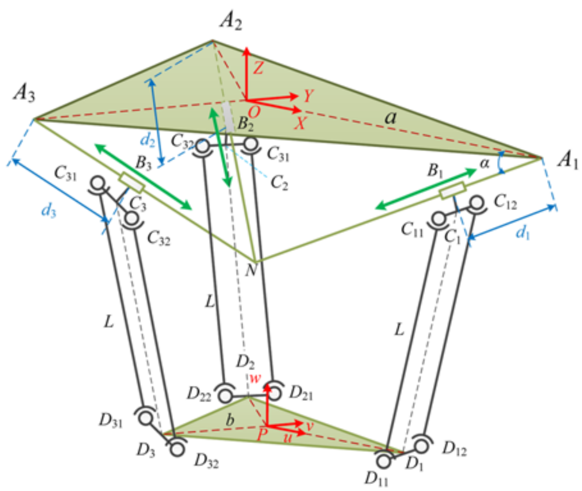

Fig. 3 Schematic diagram of the parallel robot

3. Kinematics Modelling

3.1 Architecture description

The schematic diagram of the parallel robot is shown in Fig. 3. The point B_i denotes the actuated prismatic joint. The center of ball joint (C_{ij}) that connects the leg with the slider in each of the three chains is denoted as C_i, and the center of the ball joint (D_{ij}) connected to the moving platform is denoted as D_i, where $i = 1, 2, 3$ and $j = 1, 2$. A global reference system O-XYZ is located at the center of the regular triangle $A_1A_2A_3$ with the Z-axis normal to the base and the X-axis directed along OA_1. Another local reference system P-uvw is located at the center of the regular triangle $D_1D_2D_3$. The w-axis is perpendicular to the moving platform and u-axis directed along PD_1. Related geometric parameters are $OA_i = a$, $PD_i = b$, $B_iC_i = c$, $C_iD_i = l$ and $\angle OA_iN = \alpha$.

3.2 Inverse kinematics

The position analysis is used to define a mapping from the position of reference point P in the global reference system to the set of inputs d_i. According to Fig. 3, a vector loop can be written as:

$$\overrightarrow{OP_i} + \overrightarrow{PD_i} = \overrightarrow{OA_i} + \overrightarrow{A_iB_i} + \overrightarrow{B_iC_i} + \overrightarrow{C_iD_i}\ , \tag{1}$$

or

$$\boldsymbol{p} + \boldsymbol{b}_i = \boldsymbol{a}_i + d_i\boldsymbol{u}_i + \boldsymbol{c}_i + l\boldsymbol{l}_i\ , \tag{2}$$

where $\boldsymbol{p} = [x, y, z]^T$ is the position vector of the moving platform, d_i and $\boldsymbol{u}_i$ are the displacement of the ith carriage with respect to the point A_i and its unit vector, $\boldsymbol{c}_i$ is the position vector of the short strut, l and $\boldsymbol{l}_i$ are the length and the unit vector of ith leg, $\boldsymbol{a}_i$ and $\boldsymbol{b}_i$ are the position vectors of points A_i and B_i measured in O-XYZ and P-uvw.

With respect to the global coordinate system, Eq. (2) gives three scalar equations. That is:

$$\begin{aligned}&\left(x + d_i\cos\alpha\cos\eta_i - R\cos\eta_i\right)^2 + \left(y + d_i\cos\alpha\sin\eta_i - R\sin\eta_i\right)^2\\&+\left(z + d_i\sin\alpha + c\cos\alpha\right)^2 = l^2\end{aligned}\ , \tag{3}$$

where $R = a - b + c\sin\alpha$ and $\eta_i = 2\ (i - 1)\ \pi\ /\ 3$.

The inputs of the parallel robot d_i can be solved from Eq. (3). It is found that there are two solutions for each chain. In this study, only the configurations as shown in Fig. 3 are considered.

3.3 Jacobian matrix

Eq. (3) can be differentiated with respect to time to obtain the velocity relationship, which leads to:

$$\boldsymbol{J}^{inv}\dot{\boldsymbol{d}} = \boldsymbol{J}^{dir}\dot{\boldsymbol{p}} \tag{4}$$

where $\dot{\boldsymbol{p}} = [\dot{x},\dot{y},\dot{z}]^T$ and $\dot{\boldsymbol{d}} = [\dot{d}_1,\dot{d}_2,\dot{d}_3]^T$ are the vectors of output velocities and actuator velocities.

$\boldsymbol{J}^{inv}$ is the inverse Jacobian matrix expressed as:

$$\boldsymbol{J}^{inv} = \mathrm{diag}\left(d_{11}, d_{22}, d_{33}\right), \tag{5}$$

where

$$d_{11} = x\cos\alpha + z\sin\alpha - a\cos\alpha + b\cos\alpha + d_1, \tag{6}$$

$$d_{22} = -\frac{1}{2}x\cos\alpha + \frac{\sqrt{3}}{2}y\cos\alpha + z\sin\alpha - a\cos\alpha + b\cos\alpha + d_2, \tag{7}$$

$$d_{33} = -\frac{1}{2}x\cos\alpha - \frac{\sqrt{3}}{2}y\cos\alpha + z\sin\alpha - a\cos\alpha + b\cos\alpha + d_3 \tag{8}$$

and $\boldsymbol{J}^{dir}$ is the direct Jacobian matrix expressed as:

$$\boldsymbol{J}^{dir} = \begin{bmatrix} x_1 & y_1 & z_1 \\ x_2 & y_2 & z_2 \\ x_3 & y_3 & z_3 \end{bmatrix}, \tag{9}$$

where

$$\begin{gathered} x_1 = -a + d_1\cos\alpha - c\sin\alpha + x + b,\ \ y_1 = y, \\ z_1 = d_1\sin\alpha + c\cos\alpha + z, \end{gathered} \tag{10}$$

$$\begin{gathered} x_2 = \frac{1}{2}a - \frac{1}{2}d_2\cos\alpha + \frac{1}{2}c\sin\alpha + x - \frac{1}{2}b, \\ y_2 = -\frac{\sqrt{3}}{2}a + \frac{\sqrt{3}}{2}d_2\cos\alpha - \frac{\sqrt{3}}{2}c\sin\alpha + y + \frac{\sqrt{3}}{2}b, \\ z_2 = d_2\sin\alpha + c\cos\alpha + z, \end{gathered} \tag{11}$$

$$\begin{gathered} x_3 = \frac{1}{2}a - \frac{1}{2}d_3\cos\alpha + \frac{1}{2}c\sin\alpha + x - \frac{1}{2}b, \\ y_3 = \frac{\sqrt{3}}{2}a - \frac{\sqrt{3}}{2}d_3\cos\alpha + \frac{\sqrt{3}}{2}c\sin\alpha + y - \frac{\sqrt{3}}{2}b, \\ z_3 = d_3\sin\alpha + c\cos\alpha + z. \end{gathered} \tag{12}$$

When the robot is away from singularities, the following velocity equation can be derived from Eq. (4):

$$\dot{\boldsymbol{p}} = \boldsymbol{J}_d\dot{\boldsymbol{d}}, \tag{13}$$

where

$$\boldsymbol{J}_d = \boldsymbol{J}^{-dir}\boldsymbol{J}^{inv} \tag{14}$$

is defined as the Jacobian matrix of the parallel robot.

3.4 Workspace analyses

Workspace of a parallel robot is one of important performances to reflect its working capacity. The workspace is defined as the space that can be achieved by the point P in the global reference system O-XYZ. A numerical approach using a search method in an anticipant area is adopted to derive the workspace.[36] By slicing the workspace into a series of sub-workspaces, the boundary of each sub-workspace is successively determined based on the bounded range of active prismatic joints and the mechanical limits of passive ball joints. The constraints of the prismatic joint position d_i and the ball joints rotation angle θ_{Si} should be set mathematically by:

$$d_{\min} \le d_i \le d_{\max},\ \ \theta_{Si} = \arccos\left(\boldsymbol{n}_{S0}\cdot\boldsymbol{n}_{Si}\right) \le \theta_{S\max}, \tag{15}$$

where $d_{\min}$ and $d_{\max}$ are the minimum and maximum lengths of the prismatic joint, $\boldsymbol{n}_{S0}$ and $\boldsymbol{n}_{Si}$ are the unit vector of base and swing leg on each ball joint, and $\theta_{S\max}$ is the permitted maximum rotation angle of the ball joint.

4. Stiffness Modelling

The external force on the moving platform can be simplified as a concentrated wrench $[\boldsymbol{F}^T, \boldsymbol{M}^T]^T$ and the corresponding deformation can be represented by a twist $[\boldsymbol{\Delta X}^T, \boldsymbol{\Delta\Theta}^T]^T$. $\boldsymbol{F} = [F_x, F_y, F_z]^T$ and $\boldsymbol{M} = [M_x, M_y, M_z]^T$. Similarly, $\boldsymbol{\Delta X} = [\Delta X_x, \Delta X_y, \Delta X_z]^T$ and $\boldsymbol{\Delta\Theta} = [\Delta\theta_x, \Delta\theta_y, \Delta\theta_z]^T$. They satisfy the following relationship:

$$\begin{bmatrix} \boldsymbol{F} \\ \boldsymbol{M} \end{bmatrix} = \boldsymbol{K}\begin{bmatrix} \Delta\boldsymbol{X} \\ \Delta\boldsymbol{\Theta} \end{bmatrix} \ \text{or}\ \begin{bmatrix} \Delta\boldsymbol{X} \\ \Delta\boldsymbol{\Theta} \end{bmatrix} = \boldsymbol{C}\begin{bmatrix} \boldsymbol{F} \\ \boldsymbol{M} \end{bmatrix}, \tag{16}$$

where $\boldsymbol{K}$ and $\boldsymbol{C}$ are called the stiffness matrix and compliance matrix, respectively.

Each chain of the parallel robot is sequentially connected by many components, including moving platform, leg system, drive system, guide system and base. During the following analysis, the moving platform and base are regarded as rigid bodies. To establish the compliance model of the parallel robot, the deformations of the moving platform due to leg system, drive system and guide system under the external workload are calculated separately. It is assumed that all deformations of the subsystems are small, these deformations can be added directly according to the linear superposition principle.[37]

4.1 Influence of leg system

Taking the drive system and the guide system as rigid bodies, the deformation of the moving platform due to the leg system is derived in this part. The leg system is composed of a leg and two ball joints at both ends and they are serially connected. As a result, the deformation factors mainly include leg and ball joints. Let f_{ij}^l and δ_{ij}^l denote the force and deformation of the jth leg in the ith chain. The deformation of leg system causes the platform to experience a twist in terms of the translational deformation $\Delta\boldsymbol{X}_l$ and rotational deformation $\Delta\boldsymbol{\Theta}_l$. According to the principle of virtual work, the following equation can be obtained:

$$\begin{bmatrix} \boldsymbol{F}^T & \boldsymbol{M}^T \end{bmatrix}\begin{bmatrix} \Delta\boldsymbol{X}_l \\ \Delta\boldsymbol{\Theta}_l \end{bmatrix} = \sum_{i=1}^{3}\sum_{j=1}^{2} f_{ij}^l\delta_{ij}^l. \tag{17}$$

In matrix format:

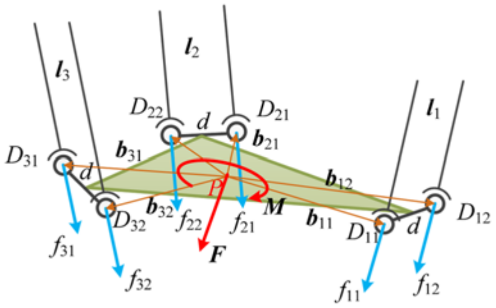

Fig. 4 Force diagram of the moving platform

$$\begin{bmatrix} \boldsymbol{F}^{\mathrm{T}} & \boldsymbol{M}^{\mathrm{T}} \end{bmatrix} \begin{bmatrix} \Delta \boldsymbol{X}_l \\ \Delta \boldsymbol{\Theta}_l \end{bmatrix} = \boldsymbol{F}_l^{\mathrm{T}} \Delta \boldsymbol{L}, \tag{18}$$

where $\boldsymbol{F}_l$ and $\Delta\boldsymbol{L}$ are the force matrix and deformation matrix of the leg system.

Based upon the Hooke's law, $\boldsymbol{F}_l$ and $\Delta\boldsymbol{l}$ have the relationships:

$$\boldsymbol{F}_l = \mathrm{diag}\left(k_{ij}^l\right)\Delta \boldsymbol{L}, \quad k_{ij}^l = \left(\frac{1}{k_{ij}^{\mathrm{le}}} + \frac{2}{k_{ij}^{\mathrm{j}}}\right)^{-1}, \tag{19}$$

where k_{ij}^l is the equivalent stiffness parameter of the jth leg system in the ith chain; $k_{ij}^{le} = \pi d_l^2 E_l / 4l$ and k_{ij}^j are the stiffness parameters of leg and ball joint, in which d_l and E_l are the diameter and elastic modulus of the leg.

The applied external wrench and reaction forces on the moving platform is shown in Fig. 4 with the relationship:

$$\begin{cases} \sum_{i=1}^{3} (f_{i1} + f_{i2}) \cdot \boldsymbol{l}_i = \boldsymbol{F} \\ \sum_{i=1}^{3} \left[f_{i1} (\boldsymbol{b}_{i1} \times \boldsymbol{l}_i) + f_{i2} (\boldsymbol{b}_{i2} \times \boldsymbol{l}_i) \right] = \boldsymbol{M} \end{cases}. \tag{20}$$

As shown in Eq. (20), $\boldsymbol{b}_{i1}$ and $\boldsymbol{b}_{i2}$ denote the vectors PD_{i1} and PD_{i2}, which can be calculated as:

$$\boldsymbol{b}_{i1} = \begin{bmatrix} b'\sin(\eta_i - \gamma) & b'\cos(\eta_i - \gamma) & 0 \end{bmatrix}^{\mathrm{T}}, \tag{21}$$

$$\boldsymbol{b}_{i2} = \begin{bmatrix} b'\sin(\eta_i + \gamma) & b'\cos(\eta_i + \gamma) & 0 \end{bmatrix}^{\mathrm{T}}, \tag{22}$$

$$b' = \sqrt{b^2 + (d/2)^2}, \quad \gamma = \arctan\frac{d/2}{b}, \tag{23}$$

where d is the distance between two ball joints in each chain.

By combing the two equations of Eq. (20), it can also be formulated as:

$$\boldsymbol{J}_l \boldsymbol{F}_l = \begin{bmatrix} \boldsymbol{F} \\ \boldsymbol{M} \end{bmatrix}, \tag{24}$$

where,

$$\boldsymbol{J}_l = [\boldsymbol{J}_{1l} \quad \boldsymbol{J}_{2l} \quad \boldsymbol{J}_{3l}], \quad \boldsymbol{J}_{il} = \begin{bmatrix} \boldsymbol{l}_i & \boldsymbol{l}_i \\ \boldsymbol{b}_{i1} \times \boldsymbol{l}_i & \boldsymbol{b}_{i2} \times \boldsymbol{l}_i \end{bmatrix}. \tag{25}$$

Thus,

$$\boldsymbol{F}_l = \boldsymbol{J}_l^{-1} \begin{bmatrix} \boldsymbol{F} \\ \boldsymbol{M} \end{bmatrix}. \tag{26}$$

According to Eqs. (18), (19) and (26), the deformation twist of the moving platform is:

$$\begin{bmatrix} \Delta \boldsymbol{X}_l \\ \Delta \boldsymbol{\Theta}_l \end{bmatrix} = \boldsymbol{C}_l \begin{bmatrix} \boldsymbol{F} \\ \boldsymbol{M} \end{bmatrix}, \quad \boldsymbol{C}_l = \boldsymbol{J}_l^{-\mathrm{T}} \left[\mathrm{diag}\left(k_{ij}^l\right)\right]^{-1} \boldsymbol{J}_l^{-1} \tag{27}$$

where $\boldsymbol{C}_l$ is the compliance matrix of the parallel robot due to the deformation of leg system.

4.2 Influence of drive system

Taking the leg system and the guide system as rigid bodies, the deformation of the moving platform due to the drive system is derived in this part. The leg system is connected to a carriage and actuated by a drive system. The drive system uses ball screw which contains a shaft and a nut. The shaft is supported by bearings at the two ends. One end of the screw is attached to a rotary motor using a coupler. As a result, the deformation factors mainly includes coupler, bearing, screw and nut. Let f_i^d and δ_i^d represent the force and deformation of the ith carriage. The axial deformation of the drive system only causes the moving platform to experience translational deformation $\Delta\boldsymbol{X}_d$. According to the principle of virtual work, it has:

$$\boldsymbol{F}^{\mathrm{T}} \Delta \boldsymbol{X}_d = \sum_{i=1}^{3} f_i^d \delta_i^d. \tag{28}$$

In matrix format:

$$\boldsymbol{F}^{\mathrm{T}} \Delta \boldsymbol{X}_d = \boldsymbol{F}_d^{\mathrm{T}} \Delta \boldsymbol{d}, \tag{29}$$

where $\boldsymbol{F}_d$ and $\Delta\boldsymbol{d}$ are the force matrix and deformation matrix of the drive system.

Based upon the Hooke's law, $\boldsymbol{F}_d$ and $\Delta\boldsymbol{d}$ have the relationships:

$$\boldsymbol{F}_d = \mathrm{diag}\left(k_i^d\right)\Delta \boldsymbol{d}, \quad k_i^d = \left(\frac{1}{k_i^{\mathrm{c}}} + \frac{1}{k_i^{\mathrm{b}}} + \frac{1}{k_i^{\mathrm{s}}} + \frac{1}{k_i^{\mathrm{n}}}\right)^{-1}, \tag{30}$$

where k_i^d is the equivalent stiffness parameter of the drive system in ith chain and it can be modeled by a set of serially connected springs according to the mechanical structure and the end supporting conditions;[38] k_i^c, k_i^b, $k_i^s = \pi d_s^2 E_s d_m / 4 d_i (d_m - d_i)$ and k_i^n are the stiffness parameters of coupler, bearing, screw and nut, in which d_s, E_s and $d_m = d_{\max} - d_{\min}$ are the diameter, elastic modulus and maximum stroke of the screw.

The relationship between $\Delta\boldsymbol{d}$ and $\Delta\boldsymbol{X}$ depends on the Jacobian matrix $\boldsymbol{J}_d$:

$$\Delta \boldsymbol{X}_d = \boldsymbol{J}_d \Delta \boldsymbol{d}. \tag{31}$$

Substitute Eq. (31) into Eq. (29), yield:

$$\left(\boldsymbol{F}_d^{\mathrm{T}} - \boldsymbol{F}^{\mathrm{T}} \boldsymbol{J}_d\right) \Delta \boldsymbol{d} = 0. \tag{32}$$

Thus,

$$\boldsymbol{F}_d = \boldsymbol{J}_d^{\mathrm{T}} \boldsymbol{F}. \tag{33}$$

According to Eqs. (29), (30) and (33), the deformation of the moving platform is:

$$\Delta \boldsymbol{X}_d = \boldsymbol{C}_d \boldsymbol{F} \quad \boldsymbol{C}_d = \boldsymbol{J}_d \left[\mathrm{diag}\left(k_i^d\right)\right]^{-1} \boldsymbol{J}_d^{\mathrm{T}} \tag{34}$$

where $\boldsymbol{C}_d$ is the compliance matrix of the parallel robot due to the deformation of drive system.

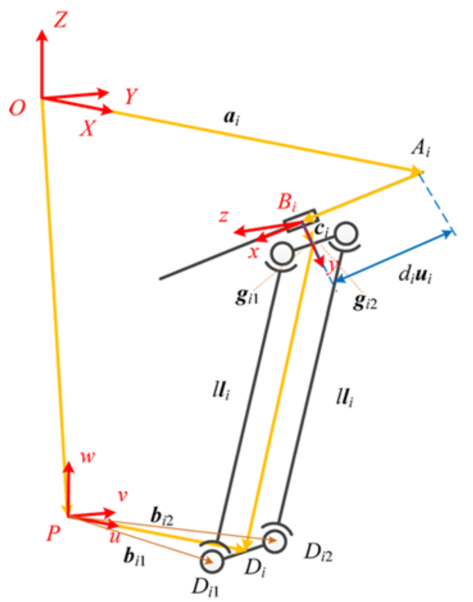

Fig. 5 Local coordinates of the carriage

4.3 Influence of guide system

Similarly, taking the leg system and the drive system as rigid bodies, the deformation of the moving platform due to the guide system can be derived. The guide system consists of a mechanism in which rail and carriage are transported by four rows of balls. As shown in Fig. 5, a local reference system B_i-xyz, is attached at the center of the carriage with x axis alone the screw direction and y axis vertical to the normal direction of carriage. In this local reference system, let $[\boldsymbol{f}_{gi}, \boldsymbol{m}_{gi}]^{\mathrm{T}}$ represent the forces on the carriage and $[\Delta\boldsymbol{x}_{gi}, \Delta\boldsymbol{\theta}_{gi}]^{\mathrm{T}}$ represent the corresponding deformations:

$$\boldsymbol{f}_i^g = \begin{bmatrix} f_{xi}^g & f_{yi}^g & f_{zi}^g \end{bmatrix}^{\mathrm{T}}, \quad \boldsymbol{m}_i^g = \begin{bmatrix} m_{xi}^g & m_{yi}^g & m_{zi}^g \end{bmatrix}^{\mathrm{T}}, \tag{35}$$

$$\Delta\boldsymbol{x}_i^g = \begin{bmatrix} \Delta x_{xi}^g & \Delta x_{yi}^g & \Delta x_{zi}^g \end{bmatrix}^{\mathrm{T}}, \quad \Delta\boldsymbol{\theta}_i^g = \begin{bmatrix} \Delta\theta_{xi}^g & \Delta\theta_{yi}^g & \Delta\theta_{zi}^g \end{bmatrix}^{\mathrm{T}}. \tag{36}$$

The deformation of guide system causes the platform to experience a twist in terms of the translational deformation $\Delta\boldsymbol{X}_g$ and rotational deformation $\Delta\boldsymbol{\Theta}_g$. According to the principle of virtual work, it has:

$$\begin{bmatrix} \boldsymbol{F}^{\mathrm{T}} & \boldsymbol{M}^{\mathrm{T}} \end{bmatrix} \begin{bmatrix} \Delta\boldsymbol{X}_g \\ \Delta\boldsymbol{\Theta}_g \end{bmatrix} = \sum_{i=1}^{3} \begin{bmatrix} \left(\boldsymbol{f}_i^g\right)^{\mathrm{T}} & \left(\boldsymbol{m}_i^g\right)^{\mathrm{T}} \end{bmatrix} \begin{bmatrix} \Delta\boldsymbol{x}_i^g \\ \Delta\boldsymbol{\theta}_i^g \end{bmatrix}. \tag{37}$$

Besides, $[(\boldsymbol{f}_i^g)^{\mathrm{T}}, (\boldsymbol{m}_i^g)^{\mathrm{T}}]^{\mathrm{T}}$ and $[(\Delta\boldsymbol{x}_i^g)^{\mathrm{T}}, (\Delta\boldsymbol{\theta}_i^g)^{\mathrm{T}}]^{\mathrm{T}}$ have the relationship:

$$\begin{bmatrix} \boldsymbol{f}_{gi} \\ \boldsymbol{m}_{gi} \end{bmatrix} = \boldsymbol{k}_{gi} \begin{bmatrix} \Delta\boldsymbol{x}_{gi} \\ \Delta\boldsymbol{\theta}_{gi} \end{bmatrix}, \quad \boldsymbol{k}_{gi} = \mathrm{diag}\left(k_{fxi}^g \quad k_{fyi}^g \quad k_{fzi}^g \quad k_{mxi}^g \quad k_{myi}^g \quad k_{mzi}^g\right), \tag{38}$$

where $\boldsymbol{k}_{gi}$ is the stiffness matrix of the guide system. k_{fxi}^g, k_{fyi}^g and k_{fzi}^g are the translational stiffness parameters alone x, y and z direction; k_{mxi}^g, k_{myi}^g and k_{mzi}^g are the rotational stiffness parameters around x, y and z direction.

According to Eqs. (38), (37) can be rearranged as:

$$\begin{bmatrix} \boldsymbol{F}^{\mathrm{T}} & \boldsymbol{M}^{\mathrm{T}} \end{bmatrix} \begin{bmatrix} \Delta\boldsymbol{X}_g \\ \Delta\boldsymbol{\Theta}_g \end{bmatrix} = \boldsymbol{F}_g^{\mathrm{T}} \Delta\boldsymbol{G}, \tag{39}$$

where

$$\boldsymbol{F}_g = \begin{bmatrix} \left(\boldsymbol{f}_1^g\right)^{\mathrm{T}} & \left(\boldsymbol{m}_1^g\right)^{\mathrm{T}} & \left(\boldsymbol{f}_2^g\right)^{\mathrm{T}} & \left(\boldsymbol{m}_2^g\right)^{\mathrm{T}} & \left(\boldsymbol{f}_3^g\right)^{\mathrm{T}} & \left(\boldsymbol{m}_3^g\right)^{\mathrm{T}} \end{bmatrix}^{\mathrm{T}}, \tag{40}$$

$$\Delta\boldsymbol{G} = \begin{bmatrix} \left(\Delta\boldsymbol{x}_1^g\right)^{\mathrm{T}} & \left(\Delta\boldsymbol{\theta}_1^g\right)^{\mathrm{T}} & \left(\Delta\boldsymbol{x}_2^g\right)^{\mathrm{T}} & \left(\Delta\boldsymbol{\theta}_2^g\right)^{\mathrm{T}} & \left(\Delta\boldsymbol{x}_3^g\right)^{\mathrm{T}} & \left(\Delta\boldsymbol{\theta}_3^g\right)^{\mathrm{T}} \end{bmatrix}^{\mathrm{T}} \tag{41}$$

represent the force matrix and deformation matrix of the guide system. $\boldsymbol{F}_g$ and $\Delta\boldsymbol{G}$ have the relationship:

$$\boldsymbol{F}_g = \boldsymbol{k}_g \Delta\boldsymbol{G}, \quad \boldsymbol{k}_g = \mathrm{diag}\left(\boldsymbol{k}_{g1} \quad \boldsymbol{k}_{g2} \quad \boldsymbol{k}_{g3}\right). \tag{42}$$

According to Fig. 5, it has the relationship:

$$\boldsymbol{p} + \boldsymbol{b}_{ij} = \boldsymbol{a}_i + d_i\boldsymbol{u}_i + \boldsymbol{c}_i + \boldsymbol{g}_{ij} + l\boldsymbol{l}_i, \tag{43}$$

where $\boldsymbol{c}_i + \boldsymbol{g}_{ij}$ represent the position vector of the jth ball joint in the ith chain represented in the reference system B_i-xyz.

Take the differential of Eq. (43), it has the relationship:

$$\begin{aligned} &\boldsymbol{p} + \Delta\boldsymbol{X}_g + \boldsymbol{b}_{ij} + \Delta\boldsymbol{\Theta}_g \times \boldsymbol{b}_{ij} \\ &= \boldsymbol{a}_i + d_i\boldsymbol{u}_i + \boldsymbol{c}_i + \boldsymbol{g}_{ij} + \boldsymbol{R}_i\left[\Delta\boldsymbol{x}_{gi} + \Delta\boldsymbol{\theta}_{gi} \times \left(\boldsymbol{c}_i + \boldsymbol{g}_{ij}\right)\right] + l\boldsymbol{l}_i + l\left(\Delta\boldsymbol{\Theta}_g \times \boldsymbol{l}_i\right) \end{aligned}, \tag{44}$$

where, $\boldsymbol{R}_i$ is the transformation matrix of the reference system B_i-xyz to the reference system O-XYZ.

Substrate Eq. (44) by Eq. (43), Eq. (45) can be obtained:

$$\Delta\boldsymbol{X}_g + \Delta\boldsymbol{\Theta}_g \times \boldsymbol{b}_{ij} = \boldsymbol{R}_i\left[\Delta\boldsymbol{x}_{gi} + \Delta\boldsymbol{\theta}_{gi} \times \left(\boldsymbol{c}_i + \boldsymbol{g}_{ij}\right)\right] + l\left(\Delta\boldsymbol{\Theta}_g \times \boldsymbol{l}_i\right). \tag{45}$$

Multiplying both side of Eq. (45) by $\boldsymbol{l}_i$, and assembling in matrix format yields:

$$\begin{bmatrix} \boldsymbol{l}_i^{\mathrm{T}} & \left(\boldsymbol{b}_{ij} \times \boldsymbol{l}_i\right)^{\mathrm{T}} \end{bmatrix} \begin{bmatrix} \Delta\boldsymbol{X}_g \\ \Delta\boldsymbol{\Theta}_g \end{bmatrix} = \begin{bmatrix} \left(\boldsymbol{R}_i^{\mathrm{T}}\boldsymbol{l}_i\right)^{\mathrm{T}} & \left(\left(\boldsymbol{c}_i + \boldsymbol{g}_{ij}\right) \times \left(\boldsymbol{R}_i^{\mathrm{T}}\boldsymbol{l}_i\right)\right)^{\mathrm{T}} \end{bmatrix} \begin{bmatrix} \Delta\boldsymbol{x}_{gi} \\ \Delta\boldsymbol{\theta}_{gi} \end{bmatrix}. \tag{46}$$

Assembling the three chain in matrix format gets:

$$\boldsymbol{A}_g \begin{bmatrix} \Delta\boldsymbol{X}_g \\ \Delta\boldsymbol{\Theta}_g \end{bmatrix} = \boldsymbol{B}_g \Delta\boldsymbol{G}, \tag{47}$$

where

$$\boldsymbol{A}_g = \begin{bmatrix} \boldsymbol{A}_{1g} & \boldsymbol{A}_{2g} & \boldsymbol{A}_{3g} \end{bmatrix}, \quad \boldsymbol{A}_{ig} = \begin{bmatrix} \boldsymbol{l}_i & \boldsymbol{l}_i \\ \boldsymbol{b}_{i1} \times \boldsymbol{l}_i & \boldsymbol{b}_{i2} \times \boldsymbol{l}_i \end{bmatrix}, \tag{48}$$

$$\boldsymbol{B}_g = \mathrm{diag}\left(\boldsymbol{B}_{1g} \quad \boldsymbol{B}_{2g} \quad \boldsymbol{B}_{3g}\right),$$

$$\boldsymbol{B}_{ig} = \begin{bmatrix} \boldsymbol{R}_i^{\mathrm{T}}\boldsymbol{l}_i & \boldsymbol{R}_i^{\mathrm{T}}\boldsymbol{l}_i \\ \left(\boldsymbol{c}_i + \boldsymbol{g}_{i1}\right) \times \left(\boldsymbol{R}_i^{\mathrm{T}}\boldsymbol{l}_i\right) & \left(\boldsymbol{c}_i + \boldsymbol{g}_{i2}\right) \times \left(\boldsymbol{R}_i^{\mathrm{T}}\boldsymbol{l}_i\right) \end{bmatrix}^{\mathrm{T}}. \tag{49}$$

Then, the relationships can be obtained:

$$\begin{bmatrix} \Delta\boldsymbol{X}_g \\ \Delta\boldsymbol{\Theta}_g \end{bmatrix} = \boldsymbol{J}_g \Delta\boldsymbol{G}, \tag{50}$$

where

$$\boldsymbol{J}_g = \left(\boldsymbol{A}_g^{\mathrm{T}}\boldsymbol{A}_g\right)^{-1} \boldsymbol{A}_g^{\mathrm{T}} \boldsymbol{B}_g. \tag{51}$$

According to the Eq. (39), (42) and (50), the deformation of the moving platform is:

$$\begin{bmatrix} \Delta\boldsymbol{X}_g \\ \Delta\boldsymbol{\Theta}_g \end{bmatrix} = \boldsymbol{C}_g \begin{bmatrix} \boldsymbol{F} \\ \boldsymbol{M} \end{bmatrix}, \quad \boldsymbol{C}_g = \boldsymbol{J}_g \boldsymbol{k}_g^{-1} \boldsymbol{J}_g^{\mathrm{T}}, \tag{52}$$

where $\boldsymbol{C}_g$ is the compliance matrix of the parallel robot due to the deformation of guide system.

4.4 Stiffness model of parallel robot

Assuming that all deformations are small, the total deformation of the moving platform is:

$$\begin{bmatrix} \Delta \boldsymbol{X} \\ \Delta \boldsymbol{\Theta} \end{bmatrix} = \begin{bmatrix} \Delta \boldsymbol{X}_d \\ \Delta \boldsymbol{\Theta}_d \end{bmatrix} + \begin{bmatrix} \Delta \boldsymbol{X}_l \\ \Delta \boldsymbol{\Theta}_l \end{bmatrix} + \begin{bmatrix} \Delta \boldsymbol{X}_g \\ \Delta \boldsymbol{\Theta}_g \end{bmatrix}. \tag{53}$$

Substituting Eqs. (27), (34) and (52) into Eq. (53), it leads to the matrix expression:

$$\begin{bmatrix} \Delta \boldsymbol{X} \\ \Delta \boldsymbol{\Theta} \end{bmatrix} = \boldsymbol{C} \begin{bmatrix} \boldsymbol{F} \\ \boldsymbol{M} \end{bmatrix}, \tag{54}$$

where

$$\boldsymbol{C} = \left[\begin{bmatrix} \boldsymbol{C}_d & \boldsymbol{0}_{3\times3} \\ \boldsymbol{0}_{3\times3} & \boldsymbol{0}_{3\times3} \end{bmatrix} + \boldsymbol{C}_l + \boldsymbol{C}_g \right]_{6\times6}. \tag{55}$$

is the compliance matrix of the parallel robot.

5. Optimization Modelling

The purpose of optimization design is to enhance the performance indices by adjusting the structural parameters. In order to ensure that the design stiffness characteristics is satisfied with the requirements, it is desired to optimize the structural parameters with the consideration of stiffness performance.

5.1 Design parameters and objective function

The main structural parameters of the parallel robot involve the radii of fixed base (a) and moving platform (b), length of legs (l), layout angle of actuators (α) and the distance between ball joints (d). For the sake of optimization, the radius of the fixed base platform is assigned as a = 400 mm. Thus, there are four design variables remained, i.e., b, l, α, d.

The external force on the parallel robot are exerted by the serial robot. According to the mechanical characteristics of the serial robot, the intersection of the A-axis, the B-axis and the H-axis coincides with the center of the spherical bonnet to form a virtual rotation pivot. The rotation of any axis in the serial robot is equivalent to rotating the bonnet around this pivot. As the spatial position of the pivot is fixed, the contact area on the workpiece remains unchanged. As a result, the direction of force on the moving platform in the parallel robot is not affected by the posture of the serial robot and it is always along the local normal direction of the workpiece. During the polishing process, the amount of bonnet offset usually keeps constant to realize constant polishing force. As a result, the value of force acting on the parallel robot at different positions can be approximated to be the same.

To facilitate the analysis, the external force on the parallel robot is converted to a concentrated wrench $[\boldsymbol{F}^{\mathrm{T}}, \boldsymbol{M}^{\mathrm{T}}]^{\mathrm{T}}$ at the center point P on the moving platform. The concentrated wrench is only related to the position of the moving platform and the shape of the workpiece to be polished. When the workpiece is flat or the curvature is small, the moving platform of the parallel robot mainly bears the force along Z direction and the moment around X and Y direction. Since the parallel robot is arranged horizontally, the parallel robot also should subject to the gravity force of moving platform and workpiece which is along X direction. Therefore, it is preferential to ensure that the translational stiffness performance of the parallel robot along X direction and Z direction, and the rotational stiffness performance of the parallel robot around X direction and Y direction. The diagonal elements of the compliance matrix represent the pure compliance in each direction. The units of terms are mm/N for $\{c_{11}, c_{22}, c_{33}\}$, and rad/Nmm for $\{c_{44}, c_{55}, c_{66}\}$. In order to get the same unit, the rotational compliance of the parallel robot is normalized by the radius of the moving platform. Considering the application of the parallel robot in the polishing machine, the matrix $\boldsymbol{C}_p$ can be obtained by rearrange matrix $\boldsymbol{C}$:

$$\Delta \boldsymbol{X}_P = \boldsymbol{C}_P \boldsymbol{F}_P \tag{56}$$

where

$$\Delta \boldsymbol{X}_P = \begin{bmatrix} \Delta X_x & \Delta X_z & b\Delta\theta_x & b\Delta\theta_y \end{bmatrix}^{\mathrm{T}}, \tag{57}$$

$$\boldsymbol{F}_P = \begin{bmatrix} F_x & F_z & M_x/b & M_y/b \end{bmatrix}^{\mathrm{T}}, \tag{58}$$

$$\boldsymbol{C}_P = \begin{bmatrix} c_{11} & c_{13} & bc_{14} & bc_{15} \\ & c_{33} & bc_{34} & bc_{35} \\ & & b^2 c_{44} & bc_{45} \\ \text{sym} & & & b^2 c_{55} \end{bmatrix}. \tag{59}$$

To ensure the precision of the parallel robot, the maximum compliance in the workspace should be small. It follows that the maximum compliance is the most important index for the parallel robot. The compliance can be evaluated using the eigenvalue of matrix $\boldsymbol{C}_p$ which is experienced in the direction of the corresponding eigenvector. The maximum eigenvalue obtained through the conventional eigenvalue decomposition of the matrix C_p are used as index to assess the stiffness performance:[39]

$$\sigma(x_i, y_i, z_i) = \sigma_{\max}(\boldsymbol{C}_P), \tag{60}$$

where $\sigma_{\max}(\boldsymbol{C}_p)$ represent the maximum eigenvalue of $\boldsymbol{C}_p$.

As the stiffness performance of the moving platform varies with the variation of the machine positions within its workspace, workspace volume V is also taken as the performance measure for dimensional optimization. This is a multi-objective optimization problem in a given design space. A single point that minimizes all the objectives simultaneously usually does not exist. As a result, the idea of Pareto optimality is used to describe solutions for multi-objective optimization problems. Typically, there are infinitely many Pareto optimal solutions for this multi-objective problem.

One of the simplest methods for solving the multi-objective optimization problems is called the weighted sum method. It firstly assigns a weight to each objective and one can views the weights as general gauges of relative importance for each objective function. Multiply all the objective functions by weights and then sum as a function to convert the multi-objective problem to a single-objective problem. It can be proved that the solution of such a single-objective problem is a Pareto optimal solution of the original multi-objective problem. By changing the weights constantly, the method can yield every Pareto optimal point as a solution. As a result, the objective

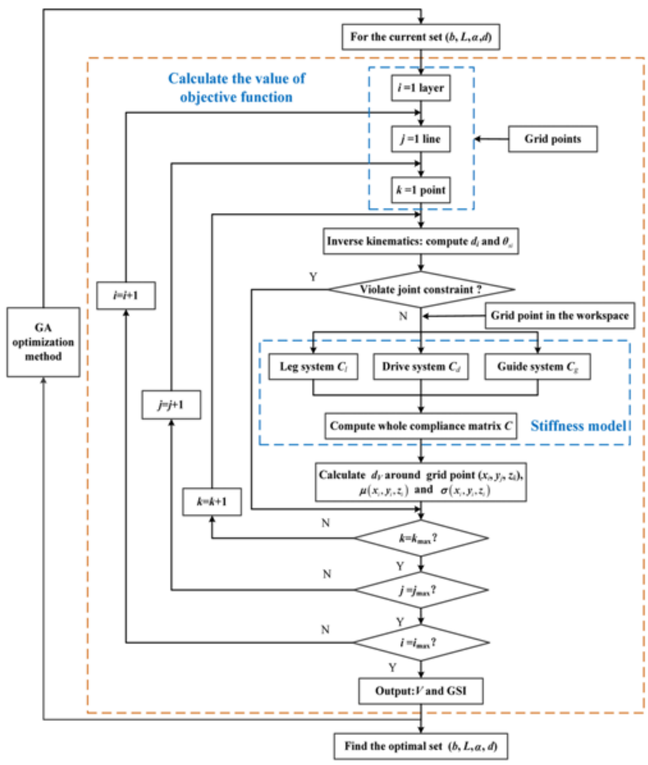

Fig. 6 Optimization procedure of the parallel robot

function is defined as:

$$\min : F(b, l, \alpha, d) = w_1 V^* + w_2 \mathrm{GSI}^*, \tag{61}$$

subject to

$$30 \text{ mm} \le b \le 120 \text{ mm}, \tag{62}$$

$$300 \text{ mm} \le l \le 500 \text{ mm}, \tag{63}$$

$$20° \le \alpha \le 70°, \tag{64}$$

$$50 \text{ mm} \le d \le 100 \text{ mm}, \tag{65}$$

where w_1 and w_2 are the weight and $w_1 + w_2 = 1$. The lower and upper limitation values of design variables are examples which are not fixed values and can be changed according to the user experience. The global stiffness index (GSI) in the workpiece is defined as:

$$\mathrm{GSI} = \frac{\int_V \sigma(x_i, y_i, z_i) \mathrm{d}V}{V}. \tag{66}$$

In order to ensure same scale, the normalized values of $V^* = -V \times 10^{-7}$ and $\mathrm{GSI}^* = 0.5 \times \mathrm{GSI} \times 10^5$ are uesd.[31]

5.2 Optimization process

The optimization process is shown in Fig. 6. For different set of (b, l, α, d), the objective function is evaluated. A cylinder with height range from -300 mm to -900 mm and radius with 400 mm is selected as the search area. The cylinder is divided into a number of layers along Z axis with a resolution of ΔZ = 5 mm. A number of grid points are then generated in each layer with a resolution of $\Delta X = \Delta Y$ = 2 mm. The active prismatic joint position d_i and passive ball angle θ_{Si} for each of the grid point are calculated by using inverse kinematics model and checked if the grid point is within the workspace. If no constraints are violated, the point is within the workspace. The workspace volume around the point is calculated and the compliance matrix is derived and recorded. After all grids are checked, the workspace volume V and global stiffness index GSI are calculated. Through a number of repetitions by using GA, the optimal set of (b, L, α, d) can be obtained.

Table 1 Structural parameters of the parallel robot

Parameter	Value	Unit
$d_{\min}$	141.4	mm
$d_{\max}$	424.3	mm
$\theta_{s\max}$	30	deg
a	400	mm
c	0	mm
d_l	30	mm
d_s	10	mm

Table 2 Stiffness coefficient of components

Parameter	Value	Unit
k^j	585	N/μm
E^l	2 × 10^{11}	N/μm^2
k^c	930	N/μm
k^b	601	N/μm
E^s	2 × 10^{11}	N/μm^2
k^n	1730	N/μm
k^g_{fxi}	980	N/μm
k^g_{fyi}	430	N/μm
k^g_{fzi}	430	N/μm
k^g_{mxi}	24	MN m/rad
k^g_{myi}	20	MN m/rad
k^g_{mzi}	20	MN m/rad

6. Results and Discussions

The major structural parameters, which are unchanged during the optimization process, are listed in Table 1. It is a set of example of the structural parameters which are mainly determined according to the size of workpiece to be polished. Table 2 gives the stiffness coefficients of joints in their local frames. These parameters are the approximate value of each components. There may exist some differences between the realistic ones. However, the main objective of this study is to optimize the structures parameters instead of precisely predicting the stiffness values and the deformations of parallel robot. Slight errors between the approximate ones and actual ones may have little effects on the final optimization results.

By solving Eqs. (55) and (59), one can obtain the compliance matrix of the parallel robot at any given positions. Table 3 shows the structural parameters associated with various sets of weights. The optimized structural values are the theoretical values based on the developed optimization model. These values are not actual values for the parallel robot, but they can be rounded and used to guide the design of the

Table 3 Optimal parameters of the parallel robot

Parameters	$w_1 = 0$	$w_1 = 0.25$	$w_1 = 0.5$	$w_1 = 0.75$	$w_1 = 1$
b (mm)	30.1	30.0	30.1	30.0	30.0
l (mm)	477.1	487.8	496.2	499.5	499.9
α (deg)	47.4	50.8	60.1	46.8	37.4
d (mm)	99.6	99.4	96.2	98.6	94.6
V*	-1.2	-1.4	-1.7	-2.8	-3.3
GSI*	1.8	2.3	3.9	4.2	4.4

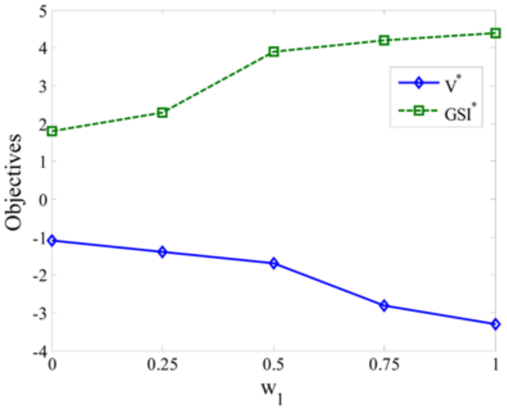

Fig. 7 Optimization results of parallel robot

realistic machine. Fig. 7 shows each of the objectives changed with the variation of weight. As shown in Fig. 7, it is found that V^* increases and GSI* decreases when w_1 varies from 0 to 1. In other words, the two objectives are conflict and a single point that minimizes all objectives simultaneously does not exist. From a mathematical point of view, this multi-objectives problems has no solution better than the others, but a set of solutions called Pareto set depends on the weight. The final choice should be made according to the user preferences. To build the machine, a specific set of structural parameters must be selected and a compromise between the criteria is inevitable. When the optimization is for maximum workspace only, i.e., $w_1 = 1$, the largest workspace volume and the highest compliance value are achieved. When the optimization is for minimizing compliance performance only, i.e., $w_1 = 0$, the lowest compliance value as well as the smallest workspace volume are obtained. It is found in Fig. 7 that the GSI* curve has the highest gradient when w_1 is between 0.25 and 0.5. If $w_1 < 0.25$, the workspace volume decreases as the compliance decreases. If $w_1 > 0.25$, the compliance deteriorates rapidly, while the workspace volume increases slow. For an ultra-precision polishing machine, the compliance performance is relatively more important than the volume of workspace. As a result, the optimal parameters obtained around $w_1 = 0.25$ are recommended to achieve a good compromise between the two objectives.

Taking the set of structural parameters at $w_1 = 0.25$ as an example, the reachable workspace of the parallel robot is generated as illustrated in Fig. 8. It can be seen that the shape of the workspace is 120° symmetric about the Z-axis. This is consistent with the global reference frame and the symmetrical structure of the parallel robot. Stiffness performance of the parallel robot cannot be discussed separately from the reference system. The distributions of stiffness performance σ (x_i, y_i,

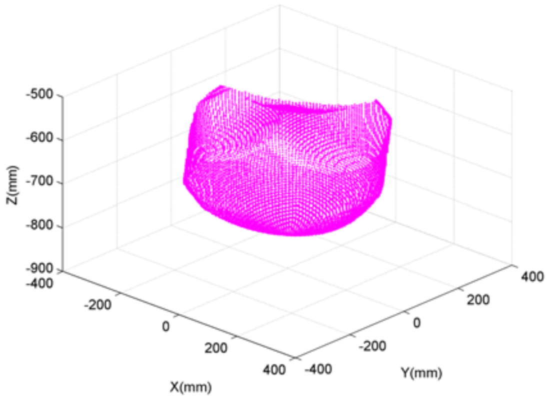

Fig. 8 Reachable workspace of the parallel robot

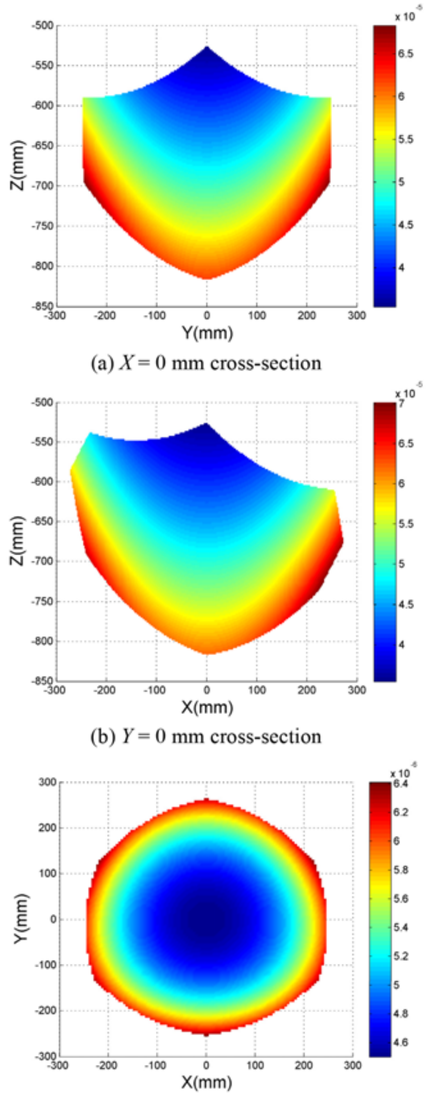

(a) $X = 0$ mm cross-section

(b) $Y = 0$ mm cross-section

(c) $Z = -650$ mm cross-section

Fig. 9 Distribution of stiffness performance σ (x_i, y_i, z_i) in the workspace

z_i) in the workspace at different cross-sections are shown in Fig. 9. As shown in Fig. 9, it is found that the workspaces at different cross-sections have different shapes and sizes. The stiffness distribution exhibits mirror symmetry in the *O-YZ* plane and 120° centrosymmetry in the *O-XY* plane. In the plane at different height alone the *Z*-axis, the minimum compliance value appears at the central position while the maximum compliance value occurs around the boundary of the workspace. Since around the boundary of the workspace, the parallel robot has a high compliance performance, it is better to restrict the parallel robot to work in a sub workspace located near the center of reachable workspace. In addition, the compliance increases with the *Z*-axis from top to button, which means the stiffness performance of the parallel robot decreases from the top to the button.

7. Conclusions

This paper presents a new polishing machine with serial and parallel robot. It is composed of a 2-DOF serial robot, a 3-DOF parallel robot as well as a turntable providing a redundant DOF. This structure takes into consideration both the characteristics of precession motion and the demand of polishing process. Due to the structural characteristics, the translational and rotational motion on the contact area between the polishing tool and workpiece are decoupled. The stiffness model of the parallel robot is established based on the inverse kinematics and Jacobian matrix considering the influence of leg system, drive system and guide system. Workspace volume of the parallel robot is obtained by an analytical method by taking into consideration of the physical joints' limits. With the objective to maximize the workspace volume and global stiffness, an optimization method is developed. By using the GA method, a set of optimal parameters are obtained. The results show that the workspace and the stiffness of this parallel robot are very sensitive to the structural parameters. For the optimized parallel robot, it has a workspace with higher stiffness performance, hence justifies its suitability for high precision polishing.

ACKNOWLEDGEMENT

This work is financial supported by the Joint Funds of the National Natural Science Foundation of China (Grant no. U1613201), the National Natural Science Foundation of China (Grant no. 51305104) and the Shenzhen Research Funds (Grants nos. SGLH201310101 44128266, JCYJ20150529141408781, and JCYJ20160427183553203). The authors would also like to express their sincere thanks to the Innovation and Technology Commission (ITC) of the Government of the Hong Kong Special Administrative Region (HKSAR) for the financial support under the Projects no. GHP/031/13SZ and a PhD studentship (project account code: RU98) provided from The Hong Kong Polytechnic University.

REFERENCES

1. Cheung, C. F., Kong, L. B., Ho, L. T., and To, S., "Modelling and Simulation of Structure Surface Generation Using Computer Controlled Ultra-Precision Polishing," Precision Engineering, Vol. 35, No. 4, pp. 574-590, 2011.
2. Lin, W., Xu, P., Li, B., and Yang, X., "Path Planning of Mechanical Polishing Process for Freeform Surface with a Small Polishing Tool," Robotics and Biomimetics, Vol. 1, No. 1, pp. 24, 2014.
3. Kumar, S., Jain, V. K., and Sidpara, A., "Nanofinishing of Freeform Surfaces (Knee Joint Implant) by Rotational-Magnetorheological Abrasive Flow Finishing (R-MRAFF) Process," Precision Engineering, Vol. 42, pp. 165-178, 2015.
4. Allen, Y. Y., Hezlep, M., and Pol, T., "A Computer Controlled Optical Pin Polishing Machine," Journal of Materials Processing Technology, Vol. 146, No. 2, pp. 156-162, 2004.
5. Kurita, T. and Hattori, M., "Development of New-Concept Desk Top Size Machine Tool," International Journal of Machine Tools and Manufacture, Vol. 45, No. 7, pp. 959-965, 2005.
6. Cheng, H.-B., Feng, Z.-J., Cheng, K., and Wang, Y.-W., "Design of a Six-Axis High Precision Machine Tool and Its Application in Machining Aspherical Optical Mirrors," International Journal of Machine Tools and Manufacture, Vol. 45, No. 9, pp. 1085-1094, 2005.
7. Zhao, J., Zhan, J., Jin, R., and Tao, M., "An Oblique Ultrasonic Polishing Method by Robot for Free-Form Surfaces," International Journal of Machine Tools and Manufacture, Vol. 40, No. 6, pp. 795-808, 2000.
8. Basanez, L. and Rosell, J., "Robotic Polishing Systems," IEEE Robotics & Automation Magazine, Vol. 12, No. 3, pp. 35-43, 2005.
9. Feng-yun, L. and Tian-sheng, L., "Development of a Robot System for Complex Surfaces Polishing Based on CL Data," The International Journal of Advanced Manufacturing Technology, Vol. 26, Nos. 9-10, pp. 1132-1137, 2005.
10. Márquez, J. J., Pérez, J. M., Rıos, J., and Vizán, A., "Process Modeling for Robotic Polishing," Journal of Materials Processing Technology, Vol. 159, No. 1, pp. 69-82, 2005.
11. Weck, M. and Staimer, D., "Parallel Kinematic Machine Tools-Current State and Future Potentials," CIRP Annals-Manufacturing Technology, Vol. 51, No. 2, pp. 671-683, 2002.
12. Lin, W., Li, B., Yang, X., and Zhang, D., "Modelling and Control of inverse Dynamics for a 5-DOF Parallel Kinematic Polishing Machine," International Journal of Advanced Robotic Systems, Vol. 10, No. 8, pp. 314, 2013.
13. Kanaan, D., Wenger, P., and Chablat, D., "Kinematic Analysis of a Serial-Parallel Machine Tool: The Verne Machine," Mechanism and Machine Theory, Vol. 44, No. 2, pp. 487-498, 2009.
14. Zhang, J., Zhao, Y., and Jin, Y., "Kinetostatic-Model-Based Stiffness Analysis of Exechon PKM," Robotics and Computer-Integrated Manufacturing, Vol. 37, pp. 208-220, 2016.
15. Cheng, G., Xu, P., Yang, D., and Liu, H., "Stiffness Analysis of a 3CPS Parallel Manipulator for Mirror Active Adjusting Platform in Segmented Telescope," Robotics and Computer-Integrated Manufacturing, Vol. 29, No. 5, pp. 302-311, 2013.

16. Xiao, S., Li, Y., and Meng, Q., "Mobility Analysis of a 3-PUU Flexure-Based Manipulator Based on Screw Theory and Compliance Matrix Method," International Journal of Precision Engineering and Manufacturing, Vol. 14, No. 8, pp. 1345-1353, 2013.

17. Klimchik, A., Chablat, D., and Pashkevich, A., "Stiffness Modeling for Perfect and Non-Perfect Parallel Manipulators Under Internal and External Loadings," Mechanism and Machine Theory, Vol. 79, pp. 1-28, 2014.

18. Yan, S., Ong, S. K., and Nee, A. Y. C., "Stiffness Analysis of Parallelogram-Type Parallel Manipulators Using a Strain Energy Method," Robotics and Computer-Integrated Manufacturing, Vol. 37, pp. 13-22, 2016.

19. Li, Y. and Xu, Q., "Stiffness Analysis for a 3-PUU Parallel Kinematic Machine," Mechanism and Machine Theory, Vol. 43, No. 2, pp. 186-200, 2008.

20. Gao, Z., Zhang, D., and Ge, Y., "Design Optimization of a Spatial Six Degree-of-Freedom Parallel Manipulator Based on Artificial Intelligence Approaches," Robotics and Computer-Integrated Manufacturing, Vol. 26, No. 2, pp. 180-189, 2010.

21. Yao, R., Tang, X., Wang, J., and Huang, P., "Dimensional Optimization Design of the Four-Cable-Driven Parallel Manipulator in Fast," IEEE/ASME Transactions on Mechatronics, Vol. 15, No. 6, pp. 932-941, 2010.

22. Hosseini, M. A. and Daniali, H. M., "Cartesian Workspace Optimization of Tricept Parallel Manipulator with Machining Application," Robotica, Vol. 33, No. 9, pp. 1948-1957, 2015.

23. Tao, Z. and An, Q., "Interference Analysis and Workspace Optimization of 3-RRR Spherical Parallel Mechanism," Mechanism and Machine Theory, Vol. 69, pp. 62-72, 2013.

24. Chi, Z., Zhang, D., Xia, L., and Gao, Z., "Multi-Objective Optimization of Stiffness and Workspace for a Parallel Kinematic Machine," International Journal of Mechanics and Materials in Design, Vol. 9, No. 3, pp. 281-293, 2013.

25. Jamwal, P. K., Xie, S., and Aw, K. C., "Kinematic Design Optimization of a Parallel Ankle Rehabilitation Robot Using Modified Genetic Algorithm," Robotics and Autonomous Systems, Vol. 57, No. 10, pp. 1018-1027, 2009.

26. Yun, Y. and Li, Y., "Optimal Design of a 3-PUPU Parallel Robot with Compliant Hinges for Micromanipulation in a Cubic Workspace," Robotics and Computer-Integrated Manufacturing, Vol. 27, No. 6, pp. 977-985, 2011.

27. Sun, T., Song, Y., Dong, G., Lian, B., and Liu, J., "Optimal Design of a Parallel Mechanism with Three Rotational Degrees of Freedom," Robotics and Computer-Integrated Manufacturing, Vol. 28, No. 4, pp. 500-508, 2012.

28. Walker, D. D., Brooks, D., King, A., Freeman, R., Morton, R., et al., "The 'Precessions' Tooling for Polishing and Figuring Flat, Spherical and Aspheric Surfaces," Optics Express, Vol. 11, No. 8, pp. 958-964, 2003.

29. Portman, V., Shneor, Y., Chapsky, V., and Shapiro, A., "Form-Shaping Function Theory Expansion: Stiffness Model of Multi-Axis Machines," The International Journal of Advanced Manufacturing Technology, Vol. 76, Nos. 5-8, pp. 1063-1078, 2015.

30. Wang, M., Liu, H., Huang, T., and Chetwynd, D. G., "Compliance Analysis of a 3-SPR Parallel Mechanism with Consideration of Gravity," Mechanism and Machine Theory, Vol. 84, pp. 99-112, 2015.

31. Jin, Y., Bi, Z. M., Liu, H. T., Higgins, C., Price, M., Chen, W. H., and Huang, T., "Kinematic Analysis and Dimensional Synthesis of Exechon Parallel Kinematic Machine for Large Volume Machining," Journal of Mechanisms and Robotics, Vol. 7, No. 4, Paper No. 041004, 2015.

32. Kakinuma, Y., Igarashi, K., Katsura, S., and Aoyama, T., "Development of 5-Axis Polishing Machine Capable of Simultaneous Trajectory, Posture, and Force Control," CIRP Annals-Manufacturing Technology, Vol. 62, No. 1, pp. 379-382, 2013.

33. Liao, L., Xi, F. J., and Liu, K., "Modeling and Control of Automated Polishing/Deburring Process Using a Dual-Purpose Compliant Toolhead," International Journal of Machine Tools and Manufacture, Vol. 48, No. 12, pp. 1454-1463, 2008.

34. Merlet, J.-P., "Parallel Robots," Springer Science & Business Media, 2012.

35. Company, O. and Pierrot, F., "Modelling and Design Issues of a 3-Axis Parallel Machine-Tool," Mechanism and Machine Theory, Vol. 37, No. 11, pp. 1325-1345, 2002.

36. Cheng, G., Qiu, B.-j., Yang, D.-h., and Liu, H.-g., "Workspace Analysis of 3-CPS Parallel Micro-Manipulator for Mirror Active Adjusting Platform," Journal of Mechanical Science and Technology, Vol. 27, No. 12, pp. 3805-3816, 2013.

37. Rao, A. B. K., Saha, S. K., and Rao, P. V. M., "Stiffness Analysis of Hexaslide Machine Tools," Advanced Robotics, Vol. 19, No. 6, pp. 671-693, 2005.

38. Chen, J.-S. and Hsu, W.-Y., "Design and Analysis of a Tripod Machine Tool with an Integrated Cartesian Guiding and Metrology Mechanism," Precision Engineering, Vol. 28, No. 1, pp. 46-57, 2004.

39. Xu, Q. and Li, Y., "An Investigation on Mobility and Stiffness of a 3-DOF Translational Parallel Manipulator via Screw Theory," Robotics and Computer-Integrated Manufacturing, Vol. 24, No. 3, pp. 402-414, 2008.